ACS Energy LETTERS

http://pubs.acs.org/journal/aelccp

Reversible Oxidative p-Doping in 2D Tin Halide Perovskite Field-Effect Transistors

Yeeun Kim,◆ Jaeyong Woo,◆ Young-Kwang Jung,◆ Heebeom Ahn, Inha Kim, Youjin Reo, Hyungbin Lim, Changjun Lee, Jonghoon Lee, Yongjin Kim, Hyeonmin Choi, Min-Hyun Lee, Jeongjae Lee, Samuel D. Stranks, Henning Sirringhaus, Yong-Young Noh,* Keehoon Kang,* and Takhee Lee*

Cite This: *ACS Energy Lett.* 2024, 9, 1725−1734

Read Online

ACCESS | Metrics & More | Article Recommendations | Supporting Information

ABSTRACT: Tin (Sn) halide perovskites are promising materials for various electronic applications due to their favorable properties. However, facile interaction with atmospheric oxygen (O_2) often hinders the practical use of Sn-based perovskites, which is regarded as a major cause of undesired variations in their electrical and structural properties. Herein, we report the reversible p-doping in phenethylammonium tin iodide ($(PEA)_2SnI_4$) transistors when they are exposed sequentially to ambient and vacuum conditions. Exposure to ambient conditions induces p-doping effects that lead to a significant shift in the threshold voltage. Interestingly, we have found that the unintentionally p-doped $(PEA)_2SnI_4$ transistors can be fully restored by simply exposing them to vacuum, indicating a complete dedoping without any structural or operational degradation. Our first-principles calculations further support the observations by revealing that the doping by O_2 molecules occurs via occupying the interstitial sites that form acceptor levels close to the valence band maximum of $(PEA)_2SnI_4$.

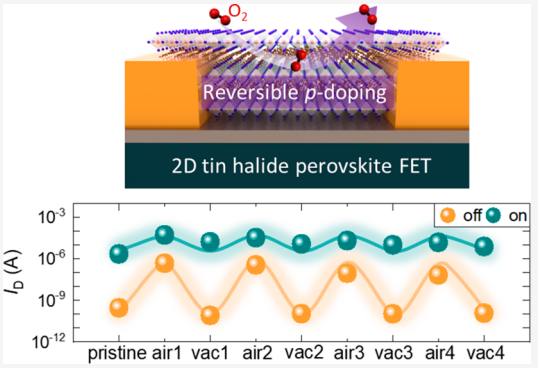

Metal halide perovskites (MHPs) have demonstrated their versatility in diverse optoelectronic fields such as solar photovoltaics, light-emitting devices, and photosensors.[1−4] The exceptional features of MHPs, including low effective mass, long carrier diffusion length, and high intrinsic carrier mobility, have opened up the possibility of using MHPs in various electronic device applications.[5−9] In particular, incorporating MHPs into field-effect transistors (FETs) provides a useful platform to better understand the carrier transport dynamics and physical properties of MHP materials under various operational conditions. Thus far, numerous studies have reported remarkable electrical properties of perovskite FETs based on diverse MHP channels, such as methylammonium lead triiodide ($MAPbI_3$), methylammonium tin iodide ($MASnI_3$), and phenethylammonium tin iodide ($(PEA)_2SnI_4$).[10−15] Among these channels, two-dimensional (2D) Sn-based perovskites have shown excellent intrinsic properties, efficient lateral charge transport, and high carrier mobility, rendering them as promising channel materials for high-performance perovskite FETs. Moreover, Sn-based perovskites are regarded as promising alternatives to Pb-based analogues, mainly due to their lower toxicity compared with Pb halide perovskites.[16] Furthermore, unlike three-dimensional (3D) counterparts, the organic spacer layers in 2D Sn halide perovskites can prevent rapid degradation in ambient conditions, enabling a progressive development of 2D Sn-based transistors.[17−21]

Despite the recent intensive progress in 2D Sn-based transistors, the practical applications of Sn halide perovskite channel materials are often hindered by their inherent susceptibility to various environmental factors, such as light, moisture, and oxygen (O_2).[2,14,22−24] In particular, atmospheric O_2 plays a pivotal role in deforming crystalline structures and forming O_2-mediated degradation products due to the low tolerance of Sn halide perovskites to O_2.[17,25−27] In addition, a rapid oxidation of Sn(II) to Sn(IV) under ambient conditions which eventually results in a p-doping significantly impedes a reliable device operation and limits our understanding of the atmospheric O_2 effects on Sn halide perovskites.[28−30] This O_2-induced evolution upon ambient conditions has necessitated a

Received: February 17, 2024
Revised: March 19, 2024
Accepted: March 19, 2024

https://doi.org/10.1021/acsenergylett.4c00497
ACS Energy Lett. 2024, 9, 1725−1734

systematic investigation into the impact of atmospheric O_2 on Sn-based perovskites.

To this end, there have been numerous studies on the interaction of the exposure of O_2 on the properties and self-doping behavior of Sn halide perovskites. The O_2 exposure effect on Sn perovskites has been discussed extensively in the context of oxidation; for example, Smith et al. investigated the in situ kinetics of Sn oxidation in 3D Sn halide perovskite thin films in different environmental conditions by real-time spectroscopic measurements.[31] Ricciarelli et al. and Lanzetta et al. provided theoretical and experimental evidence, respectively, for understanding the Sn(II)-to-Sn(IV) oxidation process and subsequent p-type self-doping effects in 3D and 2D/3D Sn perovskites upon O_2 exposure.[32,33] However, this oxidation process is mostly irreversible, often inducing a permanent change or even some damage in the film and device characteristics,[22,34] which is critical for developing industrially feasible Sn-based perovskite devices with high reliability.

On the other hand for 2D $(PEA)_2SnI_4$ perovskites, Ju et al. have reported a reversible O_2 effect on films exposed to a specific range of O_2 concentrations from photoluminescence measurements, suggesting an alternative photoactivated p-type doping pathway in Sn perovskites that can be reversible.[35] However, such a reversible doping process still remains elusive in many aspects, especially the degree of such doping, doping mechanism (i.e., exact doping sites and energetics), and their impact on charge transport in 2D perovskites. In addition, since 2D $(PEA)_2SnI_4$ perovskites have been reported as a high-mobility channel for FETs, it is imperative to directly test the impact of O_2 exposure on FET characteristics and their robustness upon complex oxidative reaction pathways.

Herein, we employ 2D layered $(PEA)_2SnI_4$ perovskite FETs for demonstrating a reversible p-doping behavior upon successive exposure to ambient and vacuum conditions. Significant p-doping effects are observed under ambient conditions in the Sn-based perovskite FETs within a few minutes, including the gradual enhancement of on- and off-current, a significant shift of threshold voltage, and an increase in mobility. This enhanced p-doping can be fully restored to its initial level by being subjected to vacuum conditions. The electrical performance of the recovered transistors, along with the results of X-ray photoelectron spectroscopy and X-ray diffraction, clearly indicates a reversible nature of the doping/dedoping effect upon atmospheric/vacuum exposure of $(PEA)_2SnI_4$ transistors without any severe structural or device degradation. The origin of the observed reversible p-doping behavior is further investigated by first-principles density functional theory (DFT) calculations to pinpoint the mechanism of a selective p-doping effect by O_2 molecules.

$(PEA)_2SnI_4$ PEROVSKITE FIELD-EFFECT TRANSISTORS AND FILM CHARACTERIZATION

To study the p-doping behavior in 2D layered Sn-based perovskites, we fabricated $(PEA)_2SnI_4$ transistors with a conventional back-gate bottom-contact structure on a 270 nm SiO_2/p^{++}-Si substrate using the spin-coating method, as presented in Figure 1a. The representative optical image of our $(PEA)_2SnI_4$ transistors is shown in Figure S1. The fabricated $(PEA)_2SnI_4$ perovskite transistors were transferred from a nitrogen (N_2)-filled glovebox to parameter-characterizing equipment using metal containers designed to minimize unintended Sn(II) oxidation by maintaining internal vacuum conditions and to protect against possible external degradation

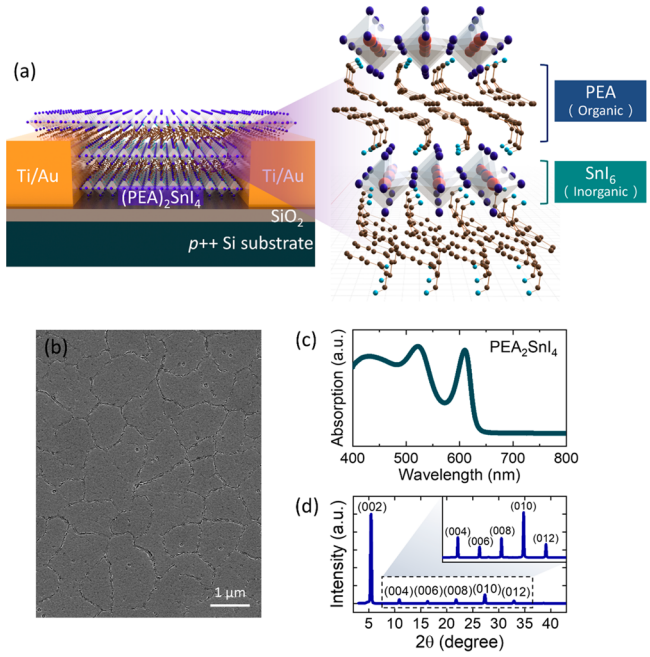

Figure 1. Device structure and film characterization. (a) Device schematic of a 2D layered $(PEA)_2SnI_4$ perovskite FET. (b) FE-SEM image, (c) UV−vis absorption spectrum, and (d) XRD pattern of $(PEA)_2SnI_4$ perovskite films.

factors, such as humidity, the surrounding gaseous environment, and light exposure. The transferred perovskite devices were placed in a vacuum chamber ($\sim 10^{-4}$ Torr) for one day before the electrical characterization to eliminate as much as possible any undesired surface adsorbates on the top surface of the $(PEA)_2SnI_4$ films. The detailed device fabrication procedure is described in the Methods section. The high polycrystalline film quality with large grain sizes (average exceeding 2 μm) of our perovskite films was confirmed by a field-emission scanning electron microscope (FE-SEM) image (Figure 1b). Figure 1c shows the ultraviolet−visible (UV−vis) absorption spectrum of a $(PEA)_2SnI_4$ film. The observed prominent absorption peaks at 434, 525, and 612 nm represent the 2D layered $(PEA)_2SnI_4$ perovskite film, which is consistent with previous reports.[36−38] In addition, the crystallinity of spin-coated perovskite films was further investigated by using X-ray diffraction (XRD) analysis (Figure 1d). The dominant (0 0 l) diffraction peaks from pristine perovskite thin film illustrate clearly the periodic stacking structure of the 2D layered $(PEA)_2SnI_4$ perovskite in which inorganic SnI_6 octahedral units sandwiched between PEA organic slabs with preferential c-axis orientation.[36,39−41] These sharp (0 0 l) peaks in XRD spectrum also imply the formation of a highly crystalline film structure with large grains in our perovskite transistors, facilitating efficient carrier transport along the perovskite channels.[42,43]

ELECTRICAL CHARACTERIZATION UNDER AMBIENT AND VACUUM CONDITIONS

We first examined the influence of ambient air exposure on our Sn-based perovskite transistors. To quantitatively investigate the air-induced changes in conduction properties of $(PEA)_2SnI_4$ FETs, the ambient exposure time evolution of the drain current versus gate voltage (I_D-V_{BG}) transfer characteristic curves are shown in Figure 2a. The increase in

https://doi.org/10.1021/acsenergylett.4c00497
ACS Energy Lett. 2024, 9, 1725−1734

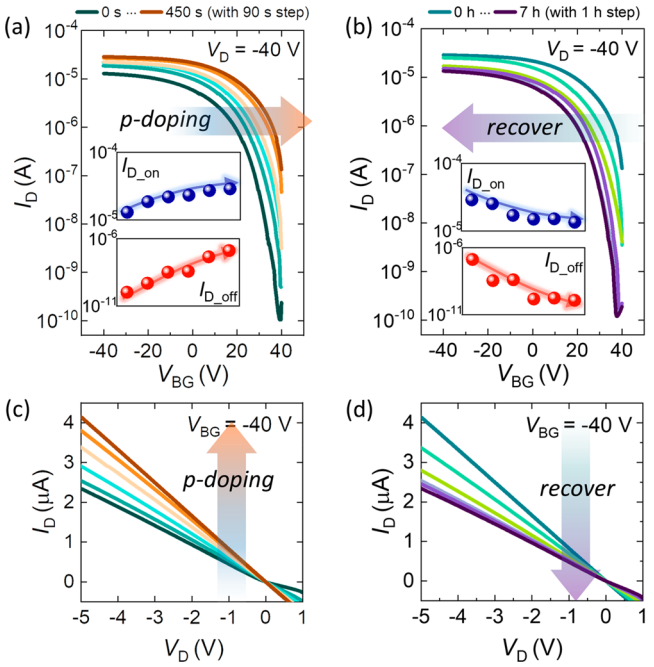

Figure 2. Effect of successive ambient air and vacuum exposure on device performance. Semilogarithmic scale I_D−V_{BG} curves at V_D = −40 V upon (a) ambient air and (b) vacuum exposure. (a, b) The insets show the variation of I_{D_on} and I_{D_off} with varying ambient air and vacuum exposure time, respectively. I_D−V_D curves at V_{BG} = −40 V upon (c) ambient air and (d) vacuum conditions.

I_D with a decreasing V_{BG} indicates the dominant p-type conduction behavior of our $(PEA)_2SnI_4$ transistors. A remarkable increase in both on-current (I_{D_on}) and off-current (I_{D_off}) with an increasing ambient air exposure time clearly shows the enhanced p-type conduction in $(PEA)_2SnI_4$ perovskite channels upon air exposure (Figure 2a inset). The drain current versus drain voltage (I_D-V_D) output characteristic curves at V_{BG} = −40 V measured with an increasing ambient air exposure time ranging from 0 s (pristine) to 450 s are displayed in Figure 2c. The gradually rising I_D with increased atmospheric air exposure time indicates enhanced p-type conduction in the perovskite channel. Furthermore, continuous enhancement in measured I_D in output characteristic curves under ambient conditions manifests negligible adsorbate permeation effects in the metal-perovskite interfaces responsible for deteriorated contact quality. The I_D-V_{BG} characteristic curves with a more prolonged air exposure time are shown in Figure S2a. As air exposure time increased, the on- and off-current ratio exhibited a saturated trend at approximately 800 s of air exposure, suggesting $(PEA)_2SnI_4$ became fully p-doped due to air exposure (Figure S2b). After air exposure for 450 s, the perovskite devices were stored immediately in vacuum (~10^{-4} Torr) at room temperature.

To monitor the changes in the electrical properties of the perovskite transistors in vacuum, the transfer characteristic curves with the vacuum storage time are shown in Figure 2b. As the vacuum storage time increases, both I_{D_on} and I_{D_off} in I_D-V_{BG} transfer characteristic curves are gradually reduced and almost reverted to their initial values after 7 h of vacuum exposure, indicating a nearly complete dedoping of the Sn-based perovskite transistors. In addition, the gradual recovery observed in the output curves also suggests the removal of the cause of p-doping in the perovskite channel by exposure to vacuum conditions (Figure 2d). Besides, the almost identical I_D values, as well as the high similarity in both output and transfer characteristic curves before (pristine) and after successive exposure to atmospheric air/vacuum (recovered), demonstrate the high reversibility of the p-doping effects without significant structural and operational degradation in our Sn-based perovskite transistors (Figure S3). Although I_D of our perovskite transistors almost saturates at negative V_{BG} and devices are not turned off until large positive V_{BG}, these are not uncommon phenomena in perovskite transistors (see Section 4 in the Supporting Information); thus, our results can serve as a reasonable reference for other studies on perovskite transistors.

To comprehend the observed reversibility of p-doping in Sn-based perovskite, we compared the electrical performances among the pristine, air-exposed, and recovered perovskite transistors, as shown in Figure 3a,b. In general, p-doping under

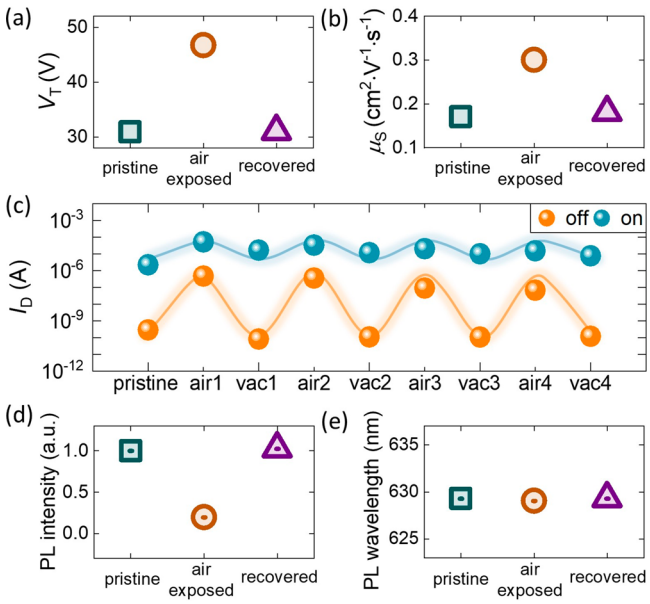

Figure 3. Restoration of electrical and PL properties in $(PEA)_2SnI_4$ perovskites upon exposure to ambient air and vacuum conditions. Comparison of (a) V_T and (b) μ_s among pristine, air-exposed, and recovered perovskite transistors. (c) Cycles of I_{D_on} and I_{D_off} at the saturation regime (V_D = −40 V) during successive ambient and vacuum exposure evolutions. Comparison of (d) the PL peak intensity normalized by maximum intensity under the pristine conditions and (e) the peak position of the PL spectra among pristine, air-exposed, and recovered perovskite films.

ambient conditions in Sn halide perovskites results from two major factors: (1) the facile oxidation of Sn(II) to Sn(IV) and (2) the substitution of O_2 molecules into native halide defects or interstitial sites within the perovskite structure. Tin vacancies (V_{Sn}) generated by oxidation of Sn(II) to Sn(IV) often cause p-doping by forming shallow acceptor levels of V_{Sn}.[5,12,32,44−46] This can disrupt the uniformity of the perovskite crystal structure and create defects that capture charge carriers in localized energy states, ultimately hindering complete reversibility and leading to significant degradation.[47] Given that the aforementioned microstructural defects arising from the Sn(II) oxidation directly influence carrier transport in perovskite channels, the negligible difference in typical transistor performance indicators, such as threshold voltage (V_T), saturation mobility ($\mu_S = (2L/WC_{OX}) \times (\partial\sqrt{I_D}/\partial V_{BG})^2$,

https://doi.org/10.1021/acsenergylett.4c00497
ACS Energy Lett. 2024, 9, 1725−1734

where L, W, and C_{OX} denote channel length, width, and oxide planar capacitance per unit area, respectively), and subthreshold swing (SS) between the pristine and the recovered transistor, implies a complete p-doping reversibility without severe structural degradation nor the formation of Sn-related defects in the $(PEA)_2SnI_4$ channel (Figure 3a,b and Figure S6). To assess the quantitative extent of the p-doping, we estimated the change of charge concentration (ΔN_A) due to the p-doping can be obtained from $\Delta N_A = C_{OX}\Delta V_T/qt_{ch}$, where ΔV_T is the shift of V_T of the device in the doped state from the pristine state (~15.8 V, from Figure 3a), q is the electric charge, and t_{ch} is the thickness of the perovskite channel (~30 nm), assuming bulk doping (discussed later). The estimated value of ΔN_A of 4.2×10^{17} cm^{-3} is consistent with the doping concentration reported previously in 2D Sn halide perovskites ($\approx 10^{14}$ to 10^{17} cm^{-3}),[48,49] closer to the high-doping range among the reported values. It is worth noting that the effective charge concentration (Δp_{eff}) can be higher by considering the insulating nature of the organic spacers of the 2D perovskites. Therefore, Δp_{eff} evaluated from ΔN_A can be estimated by assuming that the doped carriers are confined within the inorganic layers (i.e., $[SnI_6]^{4-}$ octahedral sheet in the case of $(PEA)_2SnI_4$ perovskite). The obtained value of Δp_{eff} is 1.1×10^{18} cm^{-3} which corresponds to the approximate number of carriers generated through oxidative doping per $[SnI_6]^{4-}$ octahedron to be 2.7 carriers doped per 10,000 $[SnI_6]^{4-}$ in our $(PEA)_2SnI_4$ perovskites. This discussion, although of little direct practical relevance, nevertheless provides a valuable reference for assessing the degree of the oxidative doping with various MHPs and other systems[48−51] (detailed discussion in the Supporting Information). In addition, we demonstrate the repeatability of the successful transition cycles between p-doping and dedoping in the $(PEA)_2SnI_4$ channel in Figure 3c. Each cycle of doping and dedoping involves exposing the $(PEA)_2SnI_4$ transistor to air for 300 s (represented by "air" labels in Figure 3c) followed by exposure to vacuum for 7 h (represented by "vac" labels). During the sequential exposures of the ambient air and vacuum conditions (i.e., air1, vac1, air2, vac2, etc.), the current levels changed between ~10^{-4} and ~10^{-5} A for I_{D_on} and between ~10^{-6} and ~10^{-10} A for I_{D_off}, demonstrating the repetitive nature of p-doping and dedoping processes in the perovskite transistors. Note that a slight reduction in I_{D_on} of the recovered transistor may be attributed to some inevitable air-induced degradation as the cycle progresses. We note that we fabricated other $(PEA)_2SnI_4$ transistors on different batches and confirmed the consistent electrical performance of the transistors (Figure S7). In addition, we confirmed the doping effect from measuring the photoluminescence (PL) spectra over a successive exposure to air and vacuum environments, which exhibits a similar trend to the observed reversibility in the electrical characteristics (Figure S8).[35] The PL peak intensity values among different conditions are directly compared in Figure 3d. The reduction in the PL peak intensity upon air exposure can reflect the nature of the p-doping. Figure 3e displays the PL peak position among the pristine, air-exposed, and recovered $(PEA)_2SnI_4$ films. Nearly identical PL peak positions among them indicate the absence of significant oxidative decomposition or segregation within the $(PEA)_2SnI_4$ perovskite during air exposure, which will be discussed in detail in the next section.

AIR-INDUCED DEGRADATION IN $(PEA)_2SnI_4$ PEROVSKITE

We further investigated ambient-air-dependent degradation to better understand the unavoidable influence of device degradation on the observed reversible p-doping effect. First, oxidation products such as Sn(IV) in the $(PEA)_2SnI_4$ perovskite film were investigated using X-ray photoelectron spectroscopy (XPS), as displayed in Figure S9. The relatively small difference before and after successive exposure to air and vacuum conditions in terms of the two peak positions corresponding to Sn 3d and I 3d implies the negligible generation of Sn(IV) inside the $(PEA)_2SnI_4$ perovskite film during ambient air exposure. Additionally, the nearly identical XPS spectra observed before and after electrical measurements suggest that the contribution of electrochemically induced Sn oxidation is minimal in our experiments (Figure S10). The related discussion of XPS analysis is provided in the Supporting Information. We also examined the XRD patterns of the $(PEA)_2SnI_4$ film under three different conditions to verify the absence of any significant decomposition products during air exposure (Figure S11). The absence of undefined peaks in the XRD spectrum of the $(PEA)_2SnI_4$ film under air conditions, compared to films under nitrogen (N_2) and vacuum conditions, indicates reaction pathways without any air-mediated phase segregation in the $(PEA)_2SnI_4$ film. The surface roughness of the $(PEA)_2SnI_4$ film showed minimal changes in the atomic force microscope images, and the time-of-flight secondary ion mass spectroscopy results revealed comparable levels of oxygen atoms between the pristine and the recovered film after air exposure (see Figures S12 and S13 in the Supporting Information). These findings suggest that storing the film under vacuum conditions facilitates the desorbing of the O_2 molecules in the air-exposed film and the successful recovery of the $(PEA)_2SnI_4$ film quality without deterioration. Consequently, the irreversible degradation features originating from air incorporation into the Sn-based perovskite are insignificant in our $(PEA)_2SnI_4$ transistors, allowing us to observe the repeatable reversibility of p-doping.

UNDERSTANDING THE REVERSIBLE p-Doping MECHANISM IN $(PEA)_2SnI_4$ TRANSISTORS

Now to understand the origin of reversible p-doping in our $(PEA)_2SnI_4$ transistors under ambient conditions, the fabricated transistors were exposed separately under N_2 and O_2 atmospheres. Here, the partial pressure of N_2 and O_2 was controlled at approximately 0.8 and 0.2 atm, respectively. The pristine $(PEA)_2SnI_4$ transistor was successively exposed in sequence to N_2, vacuum, O_2, and vacuum conditions for 5.5 min, 2.5 h, 6 min, and 6 h, respectively. (Figure S14). The I_D-V_{BG} transfer curves before (pristine) and after exposure to controlled N_2 conditions are compared in Figure 4a. The I_D-V_{BG} curve under N_2 conditions exhibits no certain p-doping signatures (see the blue curve for pristine and brown curve for N_2 0.8 atm in Figure 4a). Meanwhile, the clear dependence of the observed p-doping effect on O_2 conditions indicates the predominant contribution of O_2 molecules to enhanced p-type conduction in Sn-based perovskite (see blue curve for pristine and purple curve for O_2 0.2 atm in Figure S14).

Figure 4b shows the evolution of the I_D-V_{BG} transfer curves of the $(PEA)_2SnI_4$ transistor as a function of the O_2 exposure time after successive exposure under controlled N_2 and vacuum conditions. As the O_2 exposure time increases, both

https://doi.org/10.1021/acsenergylett.4c00497
ACS Energy Lett. 2024, 9, 1725−1734

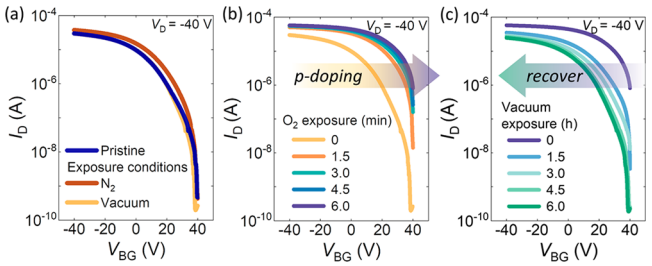

Figure 4. Effects of N_2 and O_2 on the electrical characteristic of the $(PEA)_2SnI_4$ transistor. I_D–V_{BG} curves of perovskite transistors at V_D = −40 V under (a) successive exposure in sequence to N_2 (0.8 atm), vacuum conditions, (b) 0.2 atm O_2 conditions as a function of O_2 exposure time, and (c) vacuum conditions as a function of vacuum exposure time.

I_{D_on} and I_{D_off} values gradually increase and almost reach their maximum values after 6 min (approximately 8×10^{-5} A for I_{D_on} and 10^{-6} A for I_{D_off}), which is consistent with our previous atmospheric air exposure. As expected, the observed p-doping effects progressively recover with an increasing vacuum exposure time (Figure 4c).

We also conducted similar electrical measurements under relatively humid conditions (relative humidity = 54.3%) to verify the impact of water molecules in the atmosphere on observed reversible p-doping in Sn-based perovskite. Despite ambient air containing some moisture, the hydrophobic organic spacer in $(PEA)_2SnI_4$ facilitates reversibility similar to dry O_2 exposure, but irreversibility becomes apparent under prolonged or high humidity exposure. Detailed discussions on the effect of moisture and the experimental procedure for relatively high humidity conditions are presented in Supporting Information Section 14. Notably, the consistent reversibility observed under short-term exposure to dry O_2 or ambient air and irreparable electrical performance observed after exposure to relatively high humidity conditions further support our scenario that the atmospheric O_2 (not water molecules) predominantly contributes to the repeatable reversibility of p-doping effects when the Sn-based perovskite transistors are exposed to ambient conditions.

Recent studies have shown that the O_2-adsorbates on the MHPs surface can rapidly diffuse into the bulk of MHPs within minutes (intergrain regions) or hour (to the grain interior) scale.[52] This indicates that the observed p-doping likely involves the bulk diffusion of O_2 molecules in $(PEA)_2SnI_4$. p-Doping accompanies the Fermi level of MHPs shift toward the valence band maximum (VBM), which can originate from acceptor states generated by the interaction between O_2 molecules and MHP lattice.[53,54] Considering the selective p-doping response of our Sn-based perovskite transistors to O_2 without significant structural or operational deterioration, we attribute the observed reversible p-doping to O_2 present in ambient air, rather than N_2 or H_2O molecules, for which we carried out theoretical calculations to identify the probable doping sites within the MHP lattice (the next section). Besides, the complete dedoping observed under vacuum conditions strongly supports our assumption that the interaction between the O_2 molecules and MHP lattice has a relatively low binding energy. Note that the reversibility holds up until exposure for 40 and 60 min to air and O_2, respectively, but irreversibility gradually appears after longer-term exposure to air or O_2 (Supporting Information Section 15).

DFT CALCULATIONS ON THE REVERSIBLE p-Doping EFFECT OF O_2 MOLECULES

In order to justify the observed selective p-doping by O_2 molecules under ambient exposure, we employed DFT calculations to investigate the effect of O_2 occupying (1) I vacancy or (2) interstitial sites in $(PEA)_2SnI_4$.

We first modeled I vacancies in a $\sqrt{2} \times \sqrt{2} \times 1$ supercell (376 atoms) of $(PEA)_2SnI_4$ and calculated their donor levels using the hybrid HSE06[55,56] functional with inclusion of spin–orbit coupling (SOC). Computational details can be found in the Methods Section. Due to the planar geometry of SnI_4 octahedral networks in $(PEA)_2SnI_4$, there are two distinct I vacancy sites: $V_{I,eq}$ and $V_{I,ap}$ where "eq" stands for I at the

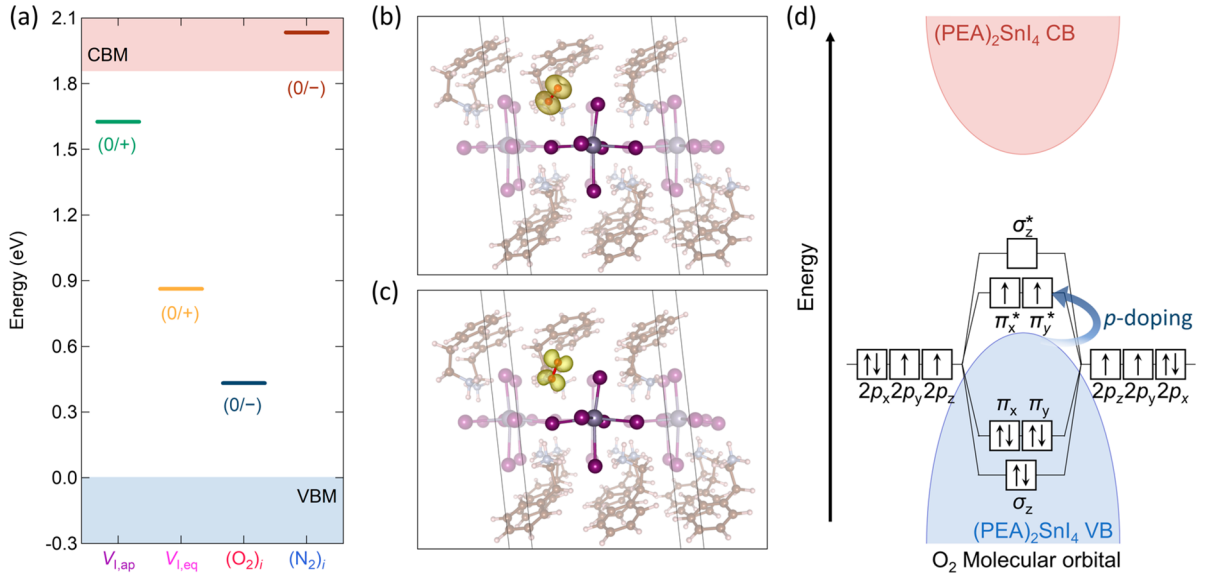

Figure 5. O_2 interstitial introduces a shallow acceptor state in the band gap of $(PEA)_2SnI_4$. (a) Calculated defect levels induced by iodine vacancies ($V_{I,ap}$ and $V_{I,eq}$), the O_2 interstitial ($(O_2)_i$), and the N_2 interstitial ($(N_2)_i$) in $(PEA)_2SnI_4$. Spin density of the interstitial O_2 with (b) neutral charge state ($(O_2)_i^0$) and (c) negative charge state ($(O_2)_i^-$). (d) Schematic of the O_2 induced p-doping mechanism.

https://doi.org/10.1021/acsenergylett.4c00497
ACS Energy Lett. 2024, 9, 1725−1734

equatorial site and "ap" stands for I at the aptical site (see Figure S20 in the Supporting Information). The calculated defect levels are shown in Figure 5a. We found that $V_{I,eq}$ induces a much deeper donor level (−1.00 eV below the CBM) than $V_{I,ap}$ (−0.24 eV below CBM), which agrees well with a previous theoretical report.[57]

Accordingly, using the same supercell and computational setups, we further modeled O_2 and N_2 interstitials (i.e., $(O_2)_i$ and $(N_2)_i$) in $(PEA)_2SnI_4$ and calculated their acceptor levels. Unlike $(O_2)_i$ in $MAPbI_3$ that induces an acceptor level close to the conduction band minimum (CBM),[53] the acceptor level induced by $(O_2)_i$ in $(PEA)_2SnI_4$ is confirmed to be close to the VBM (0.43 eV above the VBM), which can lead to p-doping. By plotting the spin densities of $(O_2)_i^0$ and $(O_2)_i^{1-}$ at their optimized geometry (Figure 5b,c), we further confirmed that the spin state of the O_2 is changed when $(O_2)_i^0$ accepts an electron and becomes $(O_2)_i^{1-}$. Figure 5d depicts a schematic diagram of the p-doping mechanism by O_2 interstitial in $(PEA)_2SnI_4$. There are two half-filled antibonding orbitals (π_x^* and π_y^*) at the ground electronic configuration of the O_2 molecule. Both the calculated acceptor level of $(O_2)_i$ close to the VBM and changes in its spin state upon accepting an electron suggest that π_x^* and π_y^* levels of O_2 are aligned slightly above the VBM of $(PEA)_2SnI_4$, which facilitates p-doping of the material. In the case of $(N_2)_i$, the calculated acceptor level is located above the CBM, because the added electron in the $(N_2)_i$ defect supercell fills empty states in the conduction band of $(PEA)_2SnI_4$, rather than filling in empty orbitals of N_2 molecules. This also explains why we could not observe any p-doping behavior of our devices under N_2 exposure. We further tested other possible O_2 sites (iodine vacancies and the intermolecular region between the PEA molecules) and their capacities for reversible p-doping; we found that O_2 molecules situated at iodine vacancy sites initiate structural degradation as opposed to the experimentally observed reversibility (Figure S21), and O_2 incorporated in the intermolecular region cannot act as a p-dopant due to an unfavorable match in energy levels (Figure S22).

To experimentally demonstrate the p-doping in $(PEA)_2SnI_4$ resulting from the O_2 molecule-induced acceptor levels, we investigated temperature-dependent p-doping effects with prolonged O_2 exposure time to 60 min at 250 K (Figure S23). We observed a significantly lower degree of p-doping at 250 K compared to that of room temperature ($\Delta p \approx 2.4 \times 10^{17}$ cm^{-3}, factor of 2 lower), despite a longer O_2 exposure time needed to saturate the doping effect (i.e., 60 min, rather than 450 s). This observation can be interpreted as the lower number of ionized O_2 molecules induced acceptor states within $(PEA)_2SnI_4$ at low temperatures.

Overall, our theoretical results reveal that the origin of the experimentally observed oxidative p-type doping/dedoping in $(PEA)_2SnI_4$ is likely to be a facile occupation/release of O_2 interstitials within $(PEA)_2SnI_4$ lattice by O_2 upon successive ambient/vacuum exposure, but note that it is difficult to experimentally confirm it through structural analysis due to several reasons: our sample is a thin film with strong preferred orientation, making high-resolution diffraction difficult if not impossible; doping concentration of oxygen is relatively low (specifically, ∼2.7 doping carriers per 10,000 perovskite octahedral, which is discussed in detail in the Supporting Information Section 6), resulting in very subtle structural changes which may be below the detection limit of commonly used structural elucidation techniques; and the sample dedopes itself in vacuum, therefore limiting the possible techniques to those conducted under atmospheric conditions.

In summary, we demonstrated a reversible p-doping effect in 2D layered $(PEA)_2SnI_4$ perovskite field-effect transistors upon exposure to ambient and vacuum conditions. As air exposure time increased, pronounced p-doping signatures such as enhanced on- and off-current levels, V_T shift, and increased carrier mobility were observed in our perovskite transistors. The observed p-doping phenomenon could be restored with vacuum exposure, showing nearly a complete dedoping in the perovskite channels without significant structural and operational degradation. In addition, the negligible variation in the XPS and XRD results as well as on- and off-current levels after repeated exposure to air/vacuum conditions demonstrated a high reversibility in the p-doping effect. We attribute this reversible p-doping effect to the facile incorporation and release of atmospheric O_2 molecules from the interstitial sites of the perovskite lattice based on the theoretical predictions by the DFT calculations which show generation of acceptor levels near VBM of $(PEA)_2SnI_4$ for justifying the selective p-doping effect by O_2. Our findings provide a basis for understanding the fundamental p-doping mechanism under ambient air conditions in Sn-based perovskites and developing advanced lead-free halide-perovskite-based electronics and optoelectronics.

METHODS

Precursor Preparation. The $(PEA)_2SnI_4$ perovskite precursor solution (0.1 M) was prepared by dissolving phenethylammonium iodide (PEAI, 100 mg/mL, purchased from Greatcell Solar Materials) and tin(II) iodide (SnI_2, 75 mg/mL, purchased from Sigma-Aldrich) in *N*,*N*′-dimethylformamide (DMF, purchased from Sigma-Aldrich) with a molar ratio of 2:1. The $(PEA)_2SnI_4$ precursor solution was stirred for 3.5 h at 60 °C before film deposition. All the processes in solution preparation were carried out in a N_2-filled glovebox.

Perovskite Field-Effect Transistor Fabrication. 270 nm thick SiO_2/p^{++}-Si substrates were sequentially cleaned using acetone, isopropanol, and deionized water for 10 min each, followed by drying in a nitrogen flow. Bottom electrodes of Au (30 nm)/Ti (3 nm) were deposited with a shadow mask on the substrates by an electron-beam evaporator (KVE-2004 L, Korea Vacuum Tech) under high-vacuum conditions (∼10^{-6} Torr) to make the active channel areas with 1000 μm × 150 μm (width × length). The substrates with bottom electrodes were cleaned again with acetone, isopropanol, and deionized water for 10 min each, and UV-ozone treatment was carried out to remove remaining surface contamination. Then, prepared perovskite solution was spin-coated at 4000 rpm for 30 s to form $(PEA)_2SnI_4$ films on the substrates, and the samples were annealed at 100 °C for 10 min in a N_2-filled glovebox.

Characterization and Electrical Measurements. The crystalline structures of $(PEA)_2SnI_4$ films were examined using X-ray diffraction (XRD) measurements (SmartLab, Rigaku and D8-Advance, Bruker). Absorbance spectra were acquired by a UV−vis spectrophotometer (V-770, JASCO). Photoluminescence (PL) spectra were measured by an XperRam 200 spectrometer (Nanobase Inc.) with a 532 nm laser as a PL excitation source. The surface images of $(PEA)_2SnI_4$ films were collected using a field-emission scanning electron microscope (FE-SEM) (GeminiSEM 560, ZEISS) at an acceleration voltage of 5 kV and an atomic force microscope (AFM) (NX-10, Park Systems). The X-ray photoelectron spectroscopy

https://doi.org/10.1021/acsenergylett.4c00497
ACS Energy Lett. 2024, 9, 1725−1734

(XPS) measurement was performed by using Axis Supra (Kratos). Depth profile of elements was measured by a time-of-flight secondary ion mass spectroscopy (TOF-SIMS) (TOF.SIMS5, IONTOF). All electrical measurements were conducted under dark conditions using a semiconductor parameter analyzer (4200-SCS, Keithley) at room temperature. FET parameters were extracted according to the methods outlined in Figure S24.

First-Principles Calculations. Underlying calculations were performed on the basis of Kohn−Sham density functional theory,[58] considering periodic boundary conditions to represent the extended crystal. The Vienna Ab Initio Simulation Package (VASP)[59,60] was employed with the projector augmented-wave (PAW)[61,62] method where the valence states of H, C, N, O, Sn, and I are treated explicitly by $1(1s^1)$, $4(2s^22p^2)$, $5(2s^22p^3)$, $6(2s^22p^4)$, $14(4d^{10}5s^25p^2)$, and $7(5s^25p^5)$ electrons, respectively. The Perdew−Burke−Ernzerhof exchange-correlation functional (PBE)[63] with the Grimme D3[64] scheme for vdW corrections (i.e., PBE + D3) was adopted to optimize the primitive unit cell and defect supercells of $(PEA)_2SnI_4$, since structural parameters of Sn-based 2D halide perovskites calculated from PBE + D3 have shown excellent agreement with experiments.[65,66] The plane-wave kinetic energy cutoff of 700 eV, a $4 \times 4 \times 1$ Γ-centered k-mesh (for the primitive cell), and a $2 \times 2 \times 1$ Γ-centered k-mesh (for supercells) were used during all structure optimization calculations. The convergence criteria were set to 10^{-6} eV and 5×10^{-2} eV Å^{-1} for total energy and atomic forces, respectively. With PBE + D3 optimized defect geometries, we accurately calculated defect levels using the Heyd−Scuseria−Ernzerhof functional (HSE06)[55,56] incorporating 43% Hartree−Fock exact exchange with spin−orbit coupling (SOC). Here, to reduce the computational cost of HSE calculations, the plane-wave kinetic energy cutoff was decreased to 500 eV and the total energy convergence criterion was lowered to 10^{-5} eV. Finite-size corrections[67,68] were also applied for charged defect supercell calculations using the dielectric constants reported by Kahmann et al.[57]

■ ASSOCIATED CONTENT

Supporting Information

The Supporting Information is available free of charge at https://pubs.acs.org/doi/10.1021/acsenergylett.4c00497.

> Optical imaging, additional characterization of $(PEA)_2SnI_4$ perovskite transistors under various environmental conditions (ambient air, vacuum, humidity, nitrogen (N_2), oxygen (O_2) under room and low temperature), comparative analyses of dual sweep and subthreshold properties upon sequential exposure to ambient air and vacuum conditions, a detailed analysis of the quantified variation in doping carrier concentration, ambient air and vacuum-induced doping effects across multiple $(PEA)_2SnI_4$ perovskite transistors, further characterization of perovskite films using an array of measurement techniques (photoluminescence (PL), X-ray Photoelectron Spectroscopy (XPS), X-ray Diffraction (XRD), Atomic Force Microscopy (AFM), and Time-of-Flight Secondary Ion Mass Spectrometry (TOF-SIMS)), and computational calculations for optimal atomic geometries for both O_2 and N_2 interstitial (PDF)

■ AUTHOR INFORMATION

Corresponding Authors

Yong-Young Noh − *Department of Chemical Engineering, Pohang University of Science and Technology (POSTECH), Pohang 37673 Gyeongbuk, Korea;* orcid.org/0000-0001-7222-2401; Email: yynoh@postech.ac.kr

Keehoon Kang − *Department of Materials Science and Engineering, Research Institute of Advanced Materials, and Institute of Applied Physics, Seoul National University, Seoul 08826, Korea*; Email: keehoon.kang@snu.ac.kr

Takhee Lee − *Department of Physics and Astronomy and Institute of Applied Physics, Seoul National University, Seoul 08826, Korea;* orcid.org/0000-0001-5988-5219; Email: tlee@snu.ac.kr

Authors

Yeeun Kim − *Department of Physics and Astronomy and Institute of Applied Physics, Seoul National University, Seoul 08826, Korea*

Jaeyong Woo − *Department of Physics and Astronomy and Institute of Applied Physics, Seoul National University, Seoul 08826, Korea*

Young-Kwang Jung − *Department of Chemical Engineering and Biotechnology, University of Cambridge, Cambridge CB3 0AS, United Kingdom;* orcid.org/0000-0003-3848-8163

Heebeom Ahn − *Department of Physics and Astronomy, Institute of Applied Physics, Department of Materials Science and Engineering, and Research Institute of Advanced Materials, Seoul National University, Seoul 08826, Korea*

Inha Kim − *Department of Physics and Astronomy and Institute of Applied Physics, Seoul National University, Seoul 08826, Korea*

Youjin Reo − *Department of Chemical Engineering, Pohang University of Science and Technology (POSTECH), Pohang 37673 Gyeongbuk, Korea*

Hyungbin Lim − *Department of Physics and Astronomy and Institute of Applied Physics, Seoul National University, Seoul 08826, Korea*

Changjun Lee − *Department of Physics and Astronomy and Institute of Applied Physics, Seoul National University, Seoul 08826, Korea*

Jonghoon Lee − *Department of Physics and Astronomy and Institute of Applied Physics, Seoul National University, Seoul 08826, Korea*

Yongjin Kim − *Department of Materials Science and Engineering, and Research Institute of Advanced Materials, Seoul National University, Seoul 08826, Korea*

Hyeonmin Choi − *Department of Materials Science and Engineering, and Research Institute of Advanced Materials, Seoul National University, Seoul 08826, Korea*

Min-Hyun Lee − *Samsung Advanced Institute of Technology (SAIT), Samsung Electronics Co. Ltd., Suwon 16678 Gyeonggi-do, Korea*

Jeongjae Lee − *School of Earth and Environmental Sciences, Seoul National University, Seoul 08826, Korea;* orcid.org/0000-0003-4294-4993

Samuel D. Stranks − *Department of Chemical Engineering and Biotechnology, University of Cambridge, Cambridge CB3 0AS, United Kingdom; Cavendish Laboratory, University of Cambridge, Cambridge CB3 0HE, United Kingdom;* orcid.org/0000-0002-8303-7292

https://doi.org/10.1021/acsenergylett.4c00497
ACS Energy Lett. 2024, 9, 1725−1734

Henning Sirringhaus − *Cavendish Laboratory, University of Cambridge, Cambridge CB3 0HE, United Kingdom;* orcid.org/0000-0001-9827-6061

Complete contact information is available at: https://pubs.acs.org/10.1021/acsenergylett.4c00497

Author Contributions

◆(Y.K., J.W., Y.-K.J.) These authors contributed equally. Y.K., J.W., Y.-Y.N., K.K., and T.L. conceived and designed the experiments. Y.-K.J. conceived and performed the computational work. Y.K., J.W., H.A, and I.K. fabricated the devices and conducted the electrical measurements. Y.K and J.W. characterized the data. J.W., H.L., and C.L. conducted and analyzed optical measurements with support from H.A. XRD, XPS, and TOF-SIMS measurements were performed by Y.K. and J.W. with support from H.A., H.L., C.L., and J.L. Yongjin.K. assists in finding relevant references and data interpretation. H.C. contributed to interpreting data for long-term air/O_2 exposure experiments in revision, and J.L. contributed to XRD experiments. Y.R. guided the device fabrication process, and M.-H.L., S.D.S., and H.S. provided advice on the overall mechanistic discussion. Y.K., J.W., Y.-K.J., Y.-Y.N., K.K., and T.L. wrote the manuscript with all of the authors. All authors contributed to the discussion and preparation of the final manuscript.

Notes

The authors declare no competing financial interest.

■ ACKNOWLEDGMENTS

The authors appreciate the financial support of the National Research Foundation of Korea (NRF) grant (No. 2021R1A2C3004783 and No. 2021R1C1C1010266), the BrainLink program (No. 2022H1D3A3A01077343), and the Nano●Material Technology Development Program grant (No. 2021M3H4A1A02049651) through NRF funded by the Ministry of Science and ICT of Korea, and the industry−university cooperation program by Samsung Electronics Co., Ltd. (IO201211-08047-01). S.D.S. acknowledges the Royal Society and Tata Group (UF150033, URF\R\221026). Y.-K.J. acknowledges UKRI guarantee funding for Marie Skłodowska-Curie Actions Postdoctoral Fellowships 2021 (EP/X025756/1). Via our membership of the UK's HEC Materials Chemistry Consortium, which is funded by EPSRC (EP/X035859/1), this work used the ARCHER2 UK National Supercomputing Service (http://www.archer2.ac.uk). This work was supported by the Research Grant from Seoul National University (0417-20230167). K.K. appreciates the support from Creative-Pioneering Researchers Program through Seoul National University.

■ REFERENCES

(1) Kim, J. S.; Heo, J. M.; Park, G. S.; Woo, S. J.; Cho, C.; Yun, H. J.; Kim, D. H.; Park, J.; Lee, S. C.; Park, S. H.; Yoon, E.; Greenham, N. C.; Lee, T. W. Ultra-Bright, Efficient and Stable Perovskite Light-Emitting Diodes. *Nature* **2022**, *611* (7937), 688−694.

(2) Cao, F.; Li, L. Progress of Lead-Free Halide Perovskites: From Material Synthesis to Photodetector Application. *Adv. Funct. Mater.* **2021**, *31* (11), 2008275.

(3) Jeong, J.; Kim, M.; Seo, J.; Lu, H.; Ahlawat, P.; Mishra, A.; Yang, Y.; Hope, M. A.; Eickemeyer, F. T.; Kim, M.; Yoon, Y. J.; Choi, I. W.; Darwich, B. P.; Choi, S. J.; Jo, Y.; Lee, J. H.; Walker, B.; Zakeeruddin, S. M.; Emsley, L.; Rothlisberger, U.; Hagfeldt, A.; Kim, D. S.; Grätzel, M.; Kim, J. Y. Pseudo-Halide Anion Engineering for α-$FAPbI_3$ Perovskite Solar Cells. *Nature* **2021**, *592* (7854), 381−385.

(4) Wang, K.; Lin, Z.-Y.; Zhang, Z.; Jin, L.; Ma, K.; Coffey, A. H.; Atapattu, H. R.; Gao, Y.; Park, J. Y.; Wei, Z.; Finkenauer, B. P.; Zhu, C.; Meng, X.; Chowdhury, S. N.; Chen, Z.; Terlier, T.; Do, T.-H.; Yao, Y.; Graham, K. R.; Boltasseva, A.; Guo, T.-F.; Huang, L.; Gao, H.; Savoie, B. M.; Dou, L. Suppressing Phase Disproportionation in Quasi-2D Perovskite Light-Emitting Diodes. *Nat. Commun.* **2023**, *14* (1), 397.

(5) Pitaro, M.; Tekelenburg, E. K.; Shao, S.; Loi, M. A. Tin Halide Perovskites: From Fundamental Properties to Solar Cells. *Adv. Mater.* **2022**, *34* (1), 2105844.

(6) Miyata, A.; Mitioglu, A.; Plochocka, P.; Portugall, O.; Wang, J. T.-W.; Stranks, S. D.; Snaith, H. J.; Nicholas, R. J. Direct Measurement of the Exciton Binding Energy and Effective Masses for Charge Carriers in Organic−Inorganic Tri-Halide Perovskites. *Nat Phys* **2015**, *11* (7), 582−587.

(7) Xing, G.; Mathews, N.; Sun, S.; Lim, S. S.; Lam, Y. M.; Grätzel, M.; Mhaisalkar, S.; Sum, T. C. Long-Range Balanced Electron- and Hole-Transport Lengths in Organic-Inorganic $CH_3NH_3PbI_3$. *Science* **2013**, *342* (6156), 344−347.

(8) Wang, Y.; Zhang, Y.; Zhang, P.; Zhang, W. High Intrinsic Carrier Mobility and Photon Absorption in the Perovskite $CH_3NH_3PbI_3$. *Phys. Chem. Chem. Phys.* **2015**, *17* (17), 11516−11520.

(9) Frost, J. M.; Butler, K. T.; Brivio, F.; Hendon, C. H.; van Schilfgaarde, M.; Walsh, A. Atomistic Origins of High-Performance in Hybrid Halide Perovskite Solar Cells. *Nano Lett.* **2014**, *14* (5), 2584−2590.

(10) She, X. J.; Chen, C.; Divitini, G.; Zhao, B.; Li, Y.; Wang, J.; Orri, J. F.; Cui, L.; Xu, W.; Peng, J.; Wang, S.; Sadhanala, A.; Sirringhaus, H. A Solvent-Based Surface Cleaning and Passivation Technique for Suppressing Ionic Defects in High-Mobility Perovskite Field-Effect Transistors. *Nat. Electron.* **2020**, *3* (11), 694−703.

(11) Senanayak, S. P.; Yang, B.; Thomas, T. H.; Giesbrecht, N.; Huang, W.; Gann, E.; Nair, B.; Goedel, K.; Guha, S.; Moya, X.; Mcneill, C. R.; Docampo, P.; Sadhanala, A.; Friend, R. H.; Sirringhaus, H. Understanding charge transport in lead iodide perovskite thin-film field-effect transistors. *Sci. Adv.* **2017**, *3*, e1601935.

(12) Zhu, H.; Liu, A.; Shim, K. I.; Jung, H.; Zou, T.; Reo, Y.; Kim, H.; Han, J. W.; Chen, Y.; Chu, H. Y.; Lim, J. H.; Kim, H. J.; Bai, S.; Noh, Y. Y. High-Performance Hysteresis-Free Perovskite Transistors through Anion Engineering. *Nat. Commun.* **2022**, *13* (1), 1741.

(13) Matsushima, T.; Hwang, S.; Sandanayaka, A. S. D.; Qin, C.; Terakawa, S.; Fujihara, T.; Yahiro, M.; Adachi, C. Solution-Processed Organic−Inorganic Perovskite Field-Effect Transistors with High Hole Mobilities. *Adv. Mater.* **2016**, *28* (46), 10275−10281.

(14) Go, J. Y.; Zhu, H.; Reo, Y.; Kim, H.; Liu, A.; Noh, Y. Y. Sodium Incorporation for Enhanced Performance of Two-Dimensional Sn-Based Perovskite Transistors. *ACS Appl. Mater. Interfaces* **2022**, *14* (7), 9363−9367.

(15) Liu, A.; Zhu, H.; Bai, S.; Reo, Y.; Zou, T.; Kim, M.-G.; Noh, Y.-Y. High-Performance Inorganic Metal Halide Perovskite Transistors. *Nat. Electron* **2022**, *5* (2), 78−83.

(16) Li, J.; Cao, H. L.; Jiao, W. B.; Wang, Q.; Wei, M.; Cantone, I.; Lü, J.; Abate, A. Biological Impact of Lead from Halide Perovskites Reveals the Risk of Introducing a Safe Threshold. *Nat. Commun.* **2020**, *11* (1), 310.

(17) Liao, Y.; Liu, H.; Zhou, W.; Yang, D.; Shang, Y.; Shi, Z.; Li, B.; Jiang, X.; Zhang, L.; Quan, L. N.; Quintero-Bermudez, R.; Sutherland, B. R.; Mi, Q.; Sargent, E. H.; Ning, Z. Highly Oriented Low-Dimensional Tin Halide Perovskites with Enhanced Stability and Photovoltaic Performance. *J. Am. Chem. Soc.* **2017**, *139* (19), 6693−6699.

(18) Lin, J. T.; Hu, Y. K.; Hou, C. H.; Liao, C. C.; Chuang, W. T.; Chiu, C. W.; Tsai, M. K.; Shyue, J. J.; Chou, P. T. Superior Stability and Emission Quantum Yield (23% ± 3%) of Single-Layer 2D Tin Perovskite TEA_2SnI_4 via Thiocyanate Passivation. *Small* **2020**, *16* (19), 2000903.

(19) Byranvand, M. M.; Zuo, W.; Imani, R.; Pazoki, M.; Saliba, M. Tin-based halide perovskite materials: Properties and applications. *Chem. Sci.* **2022**, *13*, 6766−6781.
(20) Cao, D. H.; Stoumpos, C. C.; Yokoyama, T.; Logsdon, J. L.; Song, T. B.; Farha, O. K.; Wasielewski, M. R.; Hupp, J. T.; Kanatzidis, M. G. Thin films and solar cells based on semiconducting two-dimensional Ruddlesden-Popper $(CH_3(CH2)_3NH_3)_2(CH_3NH_3)_{n-1}Sn_nI_{3n+1}$ perovskites. *ACS Energy Lett.* **2017**, *2* (5), 982−990.
(21) Shao, S.; Liu, J.; Portale, G.; Fang, H. H.; Blake, G. R.; ten Brink, G. H.; Koster, L. J. A.; Loi, M. A Highly reproducible Sn-based hybrid perovskite solar cells with 9% efficiency. *Adv. Energy Mater.* **2018**, *8* (4), 1702019.
(22) Zhang, Z.; Tian, X.; Wang, C.; Jin, J.; Jiang, Y.; Zhou, Q.; Zhu, J.; Xu, J.; He, R.; Huang, Y.; Ren, S.; Chen, C.; Gao, P.; Long, R.; Zhao, D. Revealing superoxide-induced degradation in lead-free tin perovskite solar cells. *Energy Environ. Sci.* **2022**, *15* (12), 5274−5283.
(23) Zhu, W.; Xin, G.; Scott, S. M.; Xu, W.; Yao, T.; Gong, B.; Wang, Y.; Li, M.; Lian, J. Deciphering the degradation mechanism of the lead-free all inorganic perovskite Cs_2SnI_6. *npj Mater. Degrad.* **2019**, *3* (1), 7.
(24) Noel, N. K.; Stranks, S. D.; Abate, A.; Wehrenfennig, C.; Guarnera, S.; Haghighirad, A. A.; Sadhanala, A.; Eperon, G. E.; Pathak, S. K.; Johnston, M. B.; Petrozza, A.; Herz, L. M.; Snaith, H. J. Lead-free organic-inorganic tin halide perovskites for photovoltaic applications. *Energy Environ. Sci.* **2014**, *7* (9), 3061−3068.
(25) Leijtens, T.; Prasanna, R.; Gold-Parker, A.; Toney, M. F.; McGehee, M. D. Mechanism of tin oxidation and stabilization by lead substitution in tin halide perovskites. *ACS Energy Lett.* **2017**, *2* (9), 2159−2165.
(26) Ke, J. C. R.; Lewis, D. J.; Walton, A. S.; Spencer, B. F.; O'Brien, P.; Thomas, A. G.; Flavell, W. R. Ambient-air-stable inorganic Cs_2SnI_6 double perovskite thin films: Via aerosol-assisted chemical vapour deposition. *J. Mater. Chem. A* **2018**, *6* (24), 11205−11214.
(27) Babayigit, A.; Duy Thanh, D.; Ethirajan, A.; Manca, J.; Muller, M.; Boyen, H. G.; Conings, B. Assessing the toxicity of Pb-and Sn-based perovskite solar cells in model organism Danio rerio. *Sci. Rep.* **2016**, *6*, 18721.
(28) Yu, B. B.; Chen, Z.; Zhu, Y.; Wang, Y.; Han, B.; Chen, G.; Zhang, X.; Du, Z.; He, Z. Heterogeneous 2D/3D tin-halides perovskite solar cells with certified conversion efficiency breaking 14%. *Adv. Mater.* **2021**, *33* (36), 2102055.
(29) Lanzetta, L.; Aristidou, N.; Haque, S. A. Stability of lead and tin halide perovskites: The link between defects and degradation. *J. Phys. Chem. Lett.* **2020**, *11*, 574−585.
(30) Takahashi, Y.; Hasegawa, H.; Takahashi, Y.; Inabe, T. Hall mobility in tin iodide perovskite $CH_3NH_3SnI_3$: Evidence for a doped semiconductor. *J. Solid State Chem.* **2013**, *205*, 39−43.
(31) Smith, M. A.; Chen, M.; Dai, Z.; Antolini, C.; Jayasekara, G. K.; Yadavalli, S. K.; Reinhart, B. J.; Padture, N. P.; Hayes, D. Real-time investigation of Sn(II) oxidation in Pb-free halide perovskites by X-ray absorption and Mössbauer spectroscopy. *ACS Appl. Mater. Interfaces* **2021**, *4* (5), 4327−4332.
(32) Ricciarelli, D.; Meggiolaro, D.; Ambrosio, F.; De Angelis, F. Instability of tin iodide perovskites: Bulk p-doping versus surface tin oxidation. *ACS Energy Lett.* **2020**, *5* (9), 2787−2795.
(33) Lanzetta, L.; Webb, T.; Zibouche, N.; Liang, X.; Ding, D.; Min, G.; Westbrook, R. J. E.; Gaggio, B.; Macdonald, T. J.; Islam, M. S.; Haque, S. A. Degradation mechanism of hybrid tin-based perovskite solar cells and the critical role of tin (IV) iodide. *Nat. Commun.* **2021**, *12* (1), 2853.
(34) López-Fraguas, E.; Masi, S.; Mora-Seró, I. Optical characterization of lead-free Cs_2SnI_6 double perovskite fabricated from degraded and reconstructed $CsSnI_3$ films. *ACS Appl. Energy. Mater.* **2019**, *2* (12), 8381−8387.
(35) Ju, Y.; Wu, X.-g.; Huang, S.; Dai, G.; Song, T.; Zhong, H. The evolution of photoluminescence properties of PEA_2SnI_4 upon oxygen exposure: Insight into concentration effects. *Adv. Funct. Mater.* **2022**, *32* (2), 2108296.
(36) Lanzetta, L.; Marin-Beloqui, J. M.; Sanchez-Molina, I.; Ding, D.; Haque, S. A. Two-dimensional organic tin halide perovskites with tunable visible emission and their use in light-emitting devices. *ACS Energy Lett.* **2017**, *2* (7), 1662−1668.
(37) Cai, S.; Ju, Y.; Wang, Y.; Li, X.; Guo, T.; Zhong, H.; Huang, L. Fast-response oxygen optical fiber sensor based on PEA_2SnI_4 perovskite with extremely low limit of detection. *Adv. Sci.* **2022**, *9* (8), 2104708.
(38) Yuan, F.; Zheng, X.; Johnston, A.; Wang, Y.-K.; Zhou, C.; Dong, Y.; Chen, B.; Chen, H.; Fan, J. Z.; Sharma, G.; Li, P.; Gao, Y.; Voznyy, O.; Kung, H.-T.; Lu, Z.-H.; Bakr, O. M.; Sargent, E. H. Color-pure red light-emitting diodes based on two-dimensional lead-free perovskites. *Sci. Adv.* **2020**, *6*, eabb0253.
(39) Heo, Y. J.; Jang, H. J.; Lee, J. H.; Jo, S. B.; Kim, S.; Ho, D. H.; Kwon, S. J.; Kim, K.; Jeon, I.; Myoung, J. M.; Lee, J. Y.; Lee, J. W.; Cho, J. H. Enhancing performance and stability of tin halide perovskite light emitting diodes via coordination engineering of lewis acid−base adducts. *Adv. Funct. Mater.* **2021**, *31* (51), 2106974.
(40) Cho, J. H.; Go, J. Y.; Bui, T. T.; Mun, S.; Kim, Y.; Ahn, K.; Noh, Y. Y.; Kim, M. G. Anion-vacancy-defect passivation of a 2D-layered tin-based perovskite thin-film transistor with sulfur doping. *Adv. Electron. Mater.* **2023**, *9* (3), 2201014.
(41) Kagan, C. R.; Mitzi, D. B.; Dimitrakopoulos, C. D. Organic-inorganic hybrid materials as semiconducting channels in thin-film field-effect transistors. *Science* **1999**, *286* (5441), 945−947.
(42) McGovern, L.; Koschany, I.; Grimaldi, G.; Muscarella, L. A.; Ehrler, B. Grain size influences activation energy and migration pathways in $MAPbBr_3$ perovskite solar cells. *J. Phys. Chem. Lett.* **2021**, *12* (9), 2423−2428.
(43) Wang, S.; Frisch, S.; Zhang, H.; Yildiz, O.; Mandal, M.; Ugur, N.; Jeong, B.; Ramanan, C.; Andrienko, D.; Wang, H. I.; Bonn, M.; Blom, P. W. M.; Kivala, M.; Pisula, W.; Marszalek, T. Grain engineering for improved charge carrier transport in two-dimensional lead-free perovskite field-effect transistors. *Mater. Horiz.* **2022**, *9* (10), 2633−2643.
(44) Meggiolaro, D.; Ricciarelli, D.; Alasmari, A. A.; Alasmary, F. A. S.; De Angelis, F. Tin versus lead redox chemistry modulates charge trapping and self-doping in tin/lead iodide perovskites. *J. Phys. Chem. Lett.* **2020**, *11* (9), 3546−3556.
(45) Shi, T.; Zhang, H. S.; Meng, W.; Teng, Q.; Liu, M.; Yang, X.; Yan, Y.; Yip, H. L.; Zhao, Y. J. Effects of organic cations on the defect physics of tin halide perovskites. *J. Mater. Chem. A* **2017**, *5* (29), 15124−15129.
(46) Xu, P.; Chen, S.; Xiang, H. J.; Gong, X. G.; Wei, S. H. Influence of defects and synthesis conditions on the photovoltaic performance of perovskite semiconductor $CsSnI_3$. *Chem. Mater.* **2014**, *26* (20), 6068−6072.
(47) Wong, A. B.; Bekenstein, Y.; Kang, J.; Kley, C. S.; Kim, D.; Gibson, N. A.; Zhang, D.; Yu, Y.; Leone, S. R.; Wang, L. W.; Alivisatos, A. P.; Yang, P. Strongly quantum confined colloidal cesium tin iodide perovskite nanoplates: Lessons for reducing defect density and improving stability. *Nano Lett.* **2018**, *18* (3), 2060−2066.
(48) Reo, Y.; Zhu, H.; Liu, A.; Noh, Y. Molecular doping enabling mobility boosting of 2D Sn^{2+} -based perovskites. *Adv. Funct. Mater.* **2022**, *32* (38), 2204870.
(49) Yang, S. J.; Kim, D.; Choi, J.; Kim, S. H.; Park, K.; Ryu, S.; Cho, K. Enhancing thermoelectric power factor of 2D organometal halide perovskites by suppressing 2D/3D phase separation. *Adv. Mater.* **2021**, *33* (38), 2102797.
(50) Kang, K.; Watanabe, S.; Broch, K.; Sepe, A.; Brown, A.; Nasrallah, I.; Nikolka, M.; Fei, Z.; Heeney, M.; Matsumoto, D.; Marumoto, K.; Tanaka, H.; Kuroda, S.; Sirringhaus, H. 2D coherent charge transport in highly ordered conducting polymers doped by solid state diffusion. *Nat. Mater.* **2016**, *15* (8), 896−902.
(51) Lee, J.; Baek, K.; Lee, J.; Ahn, H.; Kim, Y.; Lim, H.; Kim, Y.; Woo, J.; Stranks, S. D.; Lee, S. K.; Sirringhaus, H.; Kang, K.; Lee, T. Bulk incorporation of molecular dopants into Ruddlesden−Popper organic metal−halide perovskites for charge transfer doping. *Adv. Funct. Mater.* **2023**, *33*, 2302048.

https://doi.org/10.1021/acsenergylett.4c00497
ACS Energy Lett. 2024, 9, 1725−1734

(52) Aristidou, N.; Eames, C.; Sanchez-Molina, I.; Bu, X.; Kosco, J.; Islam, M. S.; Haque, S. A. Fast oxygen diffusion and iodide defects mediate oxygen-induced degradation of perovskite solar cells. *Nat. Commun.* **2017**, *8*, 15218.
(53) Shin, D.; Zu, F.; Cohen, A. V.; Yi, Y.; Kronik, L.; Koch, N. Mechanism and timescales of reversible p-doping of methylammonium lead triiodide by oxygen. *Adv. Mater.* **2021**, *33* (23), 2100211.
(54) Shin, D.; Zu, F.; Koch, N. Reversible oxygen-induced p-doping of mixed-cation halide perovskites. *APL Mater.* **2021**, *9* (8), No. 081104.
(55) Heyd, J.; Scuseria, G. E.; Ernzerhof, M. Hybrid functionals based on a screened Coulomb potential. *J. Chem. Phys.* **2003**, *118* (18), 8207−8215.
(56) Krukau, A. V.; Vydrov, O. A.; Izmaylov, A. F.; Scuseria, G. E. Influence of the exchange screening parameter on the performance of screened hybrid functionals. *J. Chem. Phys.* **2006**, *125* (22), 224106.
(57) Kahmann, S.; Meggiolaro, D.; Gregori, L.; Tekelenburg, E. K.; Pitaro, M.; Stranks, S. D.; De Angelis, F.; Loi, M. A. The origin of broad emission in ⟨100⟩ two-dimensional perovskites: Extrinsic vs intrinsic processes. *ACS Energy Lett.* **2022**, *7* (12), 4232−4241.
(58) Kohn, W.; Sham, L. J. Self-consistent equations including exchange and correlation effects. *Phys. Rev.* **1965**, *140*, A1133−A1138.
(59) Kresse, G.; Furthmüller, J. Efficient iterative schemes for ab initio total-energy calculations using a plane-wave basis set. *Phys. Rev. B* **1996**, *54* (16), 11169−11186.
(60) Kresse, G.; Furthmuller, J. Efficiency of ab-initio total energy calculations for metals and semiconductors using a plane-wave basis set. *Comput. Mater. Sci.* **1996**, *6*, 15−50.
(61) Kresse, G.; Joubert, D. From ultrasoft pseudopotentials to the projector augmented-wave method. *Phys. Rev. B* **1999**, *59* (3), 1758−1775.
(62) Blöchl, P. E. Projector augmented-wave method. *Phys. Rev. B* **1994**, *50* (24), 17953−17979.
(63) Perdew, J. P.; Burke, K.; Ernzerhof, M. Generalized gradient approximation made simple. *Phys. Rev. Lett.* **1997**, *78* (7), 1396.
(64) Grimme, S.; Antony, J.; Ehrlich, S.; Krieg, H. A consistent and accurate ab initio parametrization of density functional dispersion correction (DFT-D) for the 94 elements H-Pu. *J. Chem. Phys.* **2010**, *132* (15), 154104.
(65) Wang, Z.; Ganose, A. M.; Niu, C.; Scanlon, D. O. First-principles insights into tin-based two-dimensional hybrid halide perovskites for photovoltaics. *J. Mater. Chem. A* **2018**, *6* (14), 5652−5660.
(66) Ma, S.; Jung, Y.-K.; Ahn, J.; Kyhm, J.; Tan, J.; Lee, H.; Jang, G.; Lee, C. U.; Walsh, A.; Moon, J. Elucidating the origin of chiroptical activity in chiral 2D perovskites through nano-confined growth. *Nat. Commun.* **2022**, *13* (1), 3259.
(67) Kumagai, Y.; Oba, F. Electrostatics-based finite-size corrections for first-principles point defect calculations. *Phys. Rev. B* **2014**, *89* (19), 195205.
(68) Freysoldt, C.; Neugebauer, J.; Van de Walle, C. G. Fully ab initio finite-size corrections for charged-defect supercell calculations. *Phys. Rev. Lett.* **2009**, *102* (1), 16402.

https://doi.org/10.1021/acsenergylett.4c00497
ACS Energy Lett. 2024, 9, 1725−1734